Double-helical assembly of heterodimeric nanoclusters into supercrystals

https://doi.org/10.1038/s41586-021-03564-6

Yingwei Li^{1,4}, Meng Zhou^{2,4}, Yongbo Song^{3,4}, Tatsuya Higaki¹, He Wang² & Rongchao Jin^{1⊠}

Received: 31 August 2020

Accepted: 19 April 2021

Published online: 16 June 2021



Check for updates

DNA has long been used as a template for the construction of helical assemblies of inorganic nanoparticles ¹⁻⁵. For example, gold nanoparticles decorated with DNA (or with peptides) can create helical assemblies⁶⁻⁹. But without such biological ligands, helices are difficult to achieve and their mechanism of formation is challenging to understand ^{10,11}. Atomically precise nanoclusters that are protected by ligands such as thiolate 12,13 have demonstrated hierarchical structural complexity in their assembly at the interparticle and intraparticle levels, similar to biomolecules and their assemblies¹⁴. Furthermore, carrier dynamics can be controlled by engineering the structure of the nanoclusters¹⁵. But these nanoclusters usually have isotropic structures^{16,17} and often assemble into commonly found supercrystals¹⁸. Here we report the synthesis of homodimeric and heterodimeric gold nanoclusters and their self-assembly into superstructures. While the homodimeric nanoclusters form layer-by-layer superstructures, the heterodimeric nanoclusters self-assemble into double- and quadruple-helical superstructures. These complex arrangements are the result of two different motif pairs, one pair per monomer, where each motif bonds with its paired motif on a neighbouring heterodimer. This motif pairing is reminiscent of the paired interactions of nucleobases in DNA helices. Meanwhile, the $surrounding \ ligands \ on \ the \ clusters \ show \ doubly \ or \ triply \ paired \ steric \ interactions.$ The helical assembly is driven by van der Waals interactions through particle rotation and conformational matching. Furthermore, the heterodimeric clusters have a carrier lifetime that is roughly 65 times longer than that of the homodimeric clusters. Our findings suggest new approaches for increasing complexity in the structural design and engineering of precision in supercrystals.

Atomically precise, ultrasmall nanoparticles with sizes of 1–3 nm in diameter—often called nanoclusters—hold promise in elucidating many challenging issues regarding conventional nanoparticles and their assemblies 13,19,20, as the total structures of nanoclusters can be solved by single-crystal X-ray diffraction (SCXRD). Anisotropic nanoparticles (usually larger than 3 nm in diameter), or specifically heterodimeric nanoparticles, can achieve superstructures and hierarchical architectures with appreciable complexity and rich functionalities²¹⁻²⁵. In previous research on nanoclusters, however, isotropic structures were usually obtained so as to reduce the surface energy of the nanoclusters 12,16,17, and none of the reported gold nanoclusters was heterodimeric. We aim here for heterodimeric nanoclusters because their surface structures vary at different surface regions and exhibit anisotropic affinities, enabling new assembly behaviour. Crystallization of such heterodimeric nanoclusters can reveal the fundamental principles of multiscale assembly, during which the rotation of each nanocluster can achieve anisotropic interactions with neighbouring nanoclusters: the details of anisotropic interactions can be effectively recorded by crystallization, and new collective behaviour can result. The information revealed by this atomically precise approach can provide insights that extend to conventional nanoparticles and beyond.

We obtain nanoclusters of Au₂₉(SAdm)₁₉ and Au₃₀(SAdm)₁₈ (where SAdm is adamantanethiolate, SC₁₀H₁₅; see Methods and Extended Data Fig. 1a), with crystal structures solved by SCXRD (Extended Data Table 1 and Supplementary Information (Supporting CheckCIF1, CheckCIF2)). Although the difference between the two nanoclusters is 'one gold in, one thiolate (SR) out $^{'26}$, $Au_{29}(SAdm)_{19}$ shows a heterodimeric structure, whereas $Au_{30}(SAdm)_{18}$ is homodimeric, and these two nanoclusters exhibit distinctly different assembly behaviour. Interestingly, the half structure of Au₂₉(SAdm)₁₉ is identical to that of Au₃₀(SAdm)₁₈ (Fig. 1a), while the other half is the same as that of $Au_{28}(S-c-C_6H_{11})_{20}$ (ref. ²⁷). Thus, Au₂₉(SAdm)₁₉ can be regarded as a heterodimeric nanocluster inherited from two parent nanoclusters (Au₃₀ and Au₂₈, Fig. 1a), and is unique compared with the other nanoclusters reported so far. In addition to its geometric structure relationship, Au₂₉(SAdm)₁₉ is also heterodimeric in terms of its electronic structure. The numbers of free valence electrons for the two parent nanoclusters are 12 for Au₃₀(SR)₁₈ (30 - 18 = 12 electrons) and 8 for $Au_{28}(SR)_{20} (28 - 20 = 8 \text{ electrons})$.

Department of Chemistry, Carnegie Mellon University, Pittsburgh, PA, USA. 2Department of Physics, University of Miami, Coral Gables, FL, USA. 3School of Biomedical Engineering, Research and Engineering Center of Biomedical Materials, Anhui Medical University, Hefei, Anhui, China. 4These authors contributed equally: Yingwei Li, Meng Zhou, Yongbo Song [™]e-mail: rongchao@andrew.cmu.edu

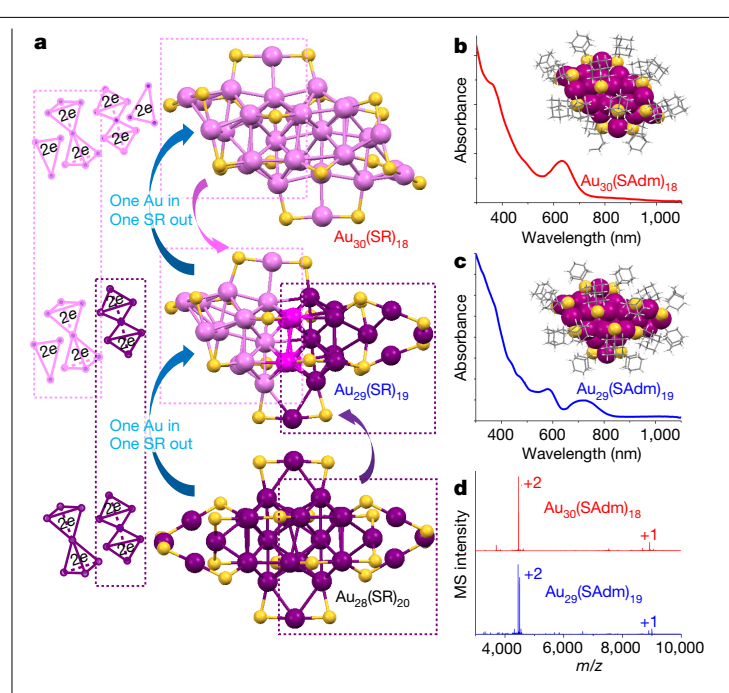


Fig. 1 | Characterization of Au₂₉(SAdm)₁₉ and Au₃₀(SAdm)₁₈ nanoclusters. a, Geometric and electronic structural evolutions achieved by the 'one gold in, one thiolate out' approach, from Au₂₈(SR)₂₀ to Au₂₉(SR)₁₉, then to Au₃₀(SR)₁₈. ${f b}, {f c}, {\sf UV-visible}$ spectra for ${\sf Au}_{30}({\sf SAdm})_{18}$ and ${\sf Au}_{29}({\sf SAdm})_{19}$ nanoclusters, with the corresponding total structures. d, ESI-MS spectra of Au₃₀(SAdm)₁₈ and Au₂₉(SAdm)₁₉. Colour codes: pink, dark pink, magenta and purple, Au; yellow, S; grey, C; white, H.

Thus, as a heterodimeric nanocluster, $Au_{29}(SR)_{19}(29-19=10 \text{ electrons})$ processes 6 electrons in one half of the structure and 4 electrons in the other half (Fig. 1a; note that each Au₄ tetrahedron contains 2 electrons).

Owing to strong quantum-size effects, both Au₃₀(SAdm)₁₈ and Au₂₉(SAdm)₁₉ show multiple molecular-like single-electron transitions in their optical absorption spectra (Fig. 1b, c), rather than the plasmons seen in metallic-state nanoparticles. We find the energy gaps between the highest occupied and lowest unoccupied molecular orbitals (the HOMO-LUMO energy gaps) to be 1.45 eV for Au₂₉(SAdm)₁₉ and 1.25 eV for Au₃₀(SAdm)₁₈ (Extended Data Fig. 1b). Electrospray ionization mass spectrometry (ESI-MS) analyses show +2 and +1 ion peaks for each of the two nanoclusters (Fig. 1d and Extended Data Fig. 1c). Note that the charges are due to ionization under ESI conditions; both nanoclusters are charge neutral in their native states.

The Au₃₀(SAdm)₁₈ structure has a face-centred-cubic (fcc) Au₂₂ kernel, which is protected by six bridging thiolates, two monomeric Au(SR)₂ staple motifs and two trimeric Au₃(SR)₄ staple motifs (Extended Data Fig. 2a, denoted L1 (monomeric) and L3 (trimeric), respectively). On the other hand, the structure of $Au_{28}(S-c-C_6H_{11})_{20}$ is composed of a fcc Au₂₀ kernel (the two missing Au atoms are marked by blue arrows in Extended Data Fig. 2a). This Au₂₀ kernel is protected by eight bridging thiolates (two additional S atoms of thiolates are marked by blue arrows in Extended Data Fig. 2b), two monomeric Au(SR)₂ staple motifs and two trimeric Au₃(SR)₄ staple motifs (Extended Data Fig. 2b, denoted C1 (monomeric) and C3 (trimeric), respectively)²⁷. As a result, when the heterodimeric $Au_{29}(SAdm)_{19}$ nanocluster is obtained, a unique structure is achieved in which a fcc Au₂₁ kernel (with one capping Au) is wrapped by four types of staple motif, namely L1, L3, C1 and C3 (Extended Data Fig. 2c).

The Au₂₉(SAdm)₁₉ nanoclusters are packed in orthorhombic space group *Pbcn*. Interestingly, when extending the unit cell along the *x* axis, the nanoclusters form double-helical patterns (Fig. 2a), with both leftand right-handedness present (Supplementary Videos 1, 2). Each pitch

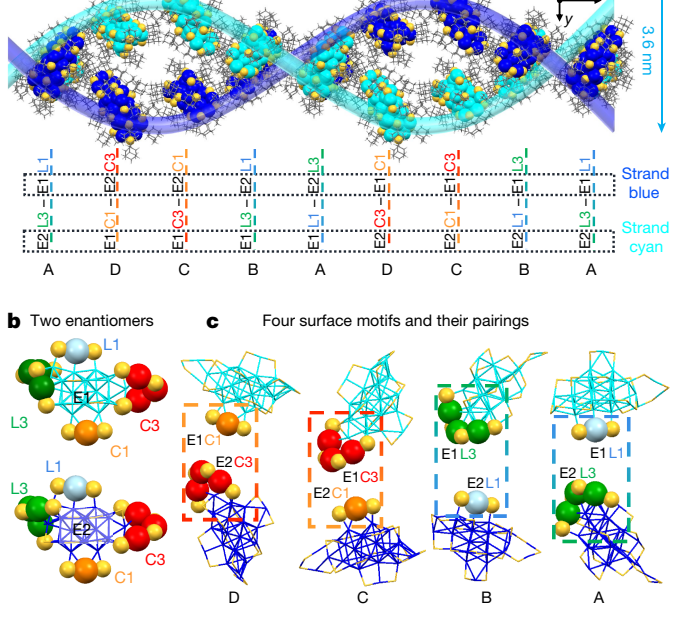


Fig. 2 | Double-helical assembly of Au₂₉ (SAdm)₁₉ nanoclusters in supercrystals. a, Self-assembly of Au₂₀(SAdm)₁₀ nanoclusters into a double-helical structure. Colour code: blue and cyan, Au in the different strands; yellow, S; grey, C; white, H. b, Two enantiomers (E1 and E2) of Au₂₉(SR)₁₉ in the supercrystal; each enantiomer contains four different staple motifs, denoted L1 and L3 (inherited from the $Au_{30}(SR)_{18}$ parent nanocluster) and C1 and C3 (inherited from the Au₂₈(SR)₂₀ parent nanocluster). **c**, Four types of motif matching between neighbouring enantiomers in the supercrystal: E1C1-E2C3 (D type), E1C3-E2C1 (C type), E1L3-E2L1 (B type) and E1L1-E2L3 (A type). The E1C1-E2C3 and E1C3-E2C1 types of motif matching are associated with triply paired ligand interactions (Extended Data Fig. 3a); the E1L3-E2L1 and E1L1-E2L3 types of motif matching are associated with doubly paired ligand interactions (Extended Data Fig. 3b). b, c, The four different staple motifs of Au₂₉(SAdm)₁₉ are marked with larger spheres of different colours.

of the double helix contains 16 nanoclusters (pitch length 12.8 nm and width 3.6 nm), and the 8 nanoclusters in each strand adopt different rotations in the assembly. The atomically precise structure allows us to identify two enantiomers of Au₂₉(SAdm)₁₉ in the supercrystal (Fig. 2b, denoted E1 and E2). Our observation of a double-helical nanocluster assembly is, to our knowledge, unprecedented. More importantly, we can further identify the origin of this assembly. In the superlattice, the two neighbouring enantiomers approach each other by matching their C1 and C3 staple motifs, or their L1 and L3 staple motifs (Fig. 2c). This is because the matched motifs come from the same parent nanocluster. Therefore, four types of interaction can be observed: E1C1-E2C3 (denoted D), E1C3-E2C1 (denoted C), E1L3-E2L1 (denoted B) and E1L1-E2L3 (denoted A). Specifically, when the C1 and C3 staple motifs pair up (Fig. 2c, D and C interactions), the ligands surrounding them are triply paired (Extended Data Fig. 3a). These triply paired ligands arrange themselves in a staggered conformation, resulting in oppositely stacked triangles owing to the steric repulsion between the bulky adamantanethiolates. When the L1 and L3 staple motifs pair up (Fig. 2c, B and A interactions), the ligands surrounding them are doubly paired (Extended Data Fig. 3b), and the doubly paired ligands interlock with each other.

The two enantiomers and four different surface motifs on the Au₂₉ nanocluster with their specific matching, as well as the doubly and triply paired ligand interactions, all contribute to the formation of the double-helical assembly of Au₂₉(SAdm)₁₉ nanoclusters. This is

reminiscent of DNA, in which there are two strands, four nucleobases (thymine, adenine, cytosine and guanine), and double or triple hydrogen bonds between the two strands. Ionic (repulsive) interactions, π - π stacking and hydrogen (attractive) bonds-being relatively strong and balanced against one another—are central to natural helical structures. In the double-helical assembly of Au₂₉(SAdm)₁₉ nanoclusters with four types of staple motif, the conformational matching (attractive) and steric repulsions (repulsive) are weak but balanced as well. To reach such a balance, van der Waals forces drive the rotation of nanoclusters in solution until their surface motifs create suitable anisotropic interactions with those of neighbouring enantiomeric nanoclusters. The 'motif pairs' in the nanocluster assembly are equivalent to the 'base pairs' in DNA structures. But as the four motifs are collected on one nanocluster, pairing has to be achieved by particle rotation in solution; the collective behaviour of all nanoclusters is then fixed during crystallization and observed by crystallography. The L1-L3 and C1-C3 pairs show the same geometry, allowing for equal distances between two strands and balanced ligand interactions; other pairs (for example, L1-C1 or L3-C3) would disturb the helix.

The information revealed in this atomically precise assembly could contribute to the fundamental understanding of protein folding and funnelling, and of the assembly of conventional nanoparticles and supramolecules. We deduce that anisotropic structures (or interactions) can be created on the surface of conventional nanoparticles, resulting in specific assemblies. Designing nanoparticles with heterostructures and paired anisotropic interactions can result in the assembly of double helices with high programmability.

To gain further insights, we also crystallized the adamantanethiolateprotected Au₃₀(SAdm)₁₈ parent nanocluster (see Supplementary Information (Supporting CheckCIF2)), because different surface motifs could substantially affect the self-assembly of nanoclusters. The Au₃₀(SAdm)₁₈ nanocluster possesses two L1 and two L3 motifs. Although two enantiomers are also found in the superlattice of such nanoclusters, no helical assembly is obtained (monoclinic space group $P2_1/n$; Extended Data Fig. 4a). The two neighbouring nanoclusters approach each other, with two L3 staple motifs matching oppositely (Extended Data Fig. 4b; that is, L3-L3), completely different from the L1-L3 or C1-C3 motif pairs in the spiral network of the Au₂₉(SAdm)₁₉ assembly, although doubly and triply paired ligands can also be identified in the Au₃₀(SAdm)₁₈ assembly. We also studied a series of adamantanethiolate-protected metal nanoclusters²⁸, but none shows a spiral pattern of assembly (Extended Data Fig. 5-8). despite the existence of doubly paired (Extended Data Figs. 5, 7), triply paired (Extended Data Figs. 6, 7) or even quadruply paired (Extended Data Fig. 8) ligands. We conclude that steric repulsion between bulky ligands (for example, doubly or triply paired ligands) is a common phenomenon in SAdm-protected nanoclusters¹⁹, but is not the key to helical assembly. Rather, the heterodimeric structure of the Au₂₉ nanocluster—in which four different surface motifs (L1, L3, C1 and C3) are half-inherited from the two parent nanoclusters—is essential for helix formation. Au₃₀(SAdm)₁₈ possesses only two L1 and two L3 motifs, hence no helical assembly.

By analysing the superlattice in a larger dimension, we can identify a quadruple helical structure, with pitch and diameter being roughly 12.8 nm and 5.3 nm, respectively (Fig. 3a and Supplementary Videos 3, 4). Each of the four strands illustrates the spiral feature in the assembly (Fig. 3b). In the ABCD layer stacking, the A or D layer contains four nanoclusters of the same chirality (E1) encircling one opposite enantiomer (E2), and each of the four motifs of the central nanocluster matches the corresponding motif of the neighbouring nanocluster of opposite chirality (Fig. 3c, left). In the B or C layer, two pairs of enantiomers reside alternatively in the circle, matching motifs in four corresponding ways (Fig. 3c, right). The L1 and L3 motifs match up in the same way as in the double helix, as do the C1 and C3 motifs. From this perspective, even larger helical structures can be expected

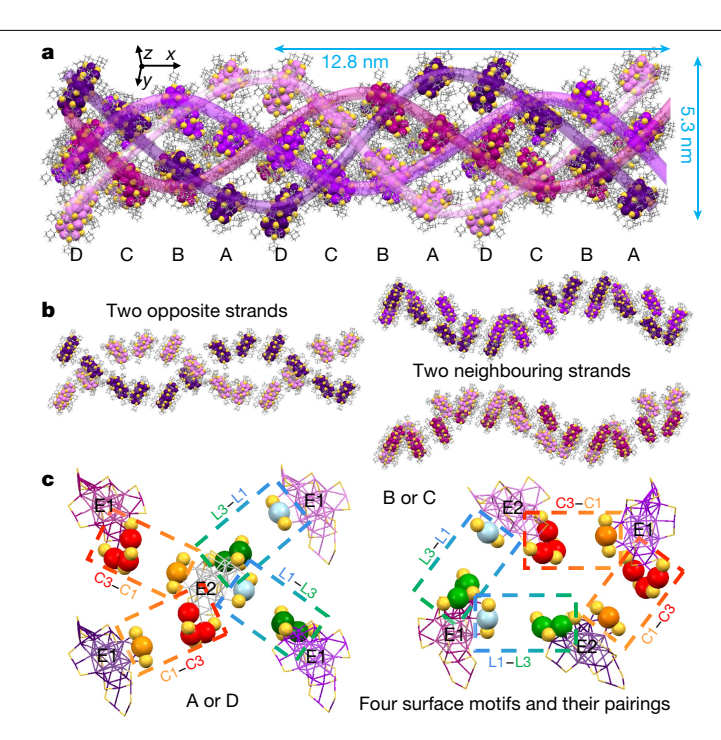
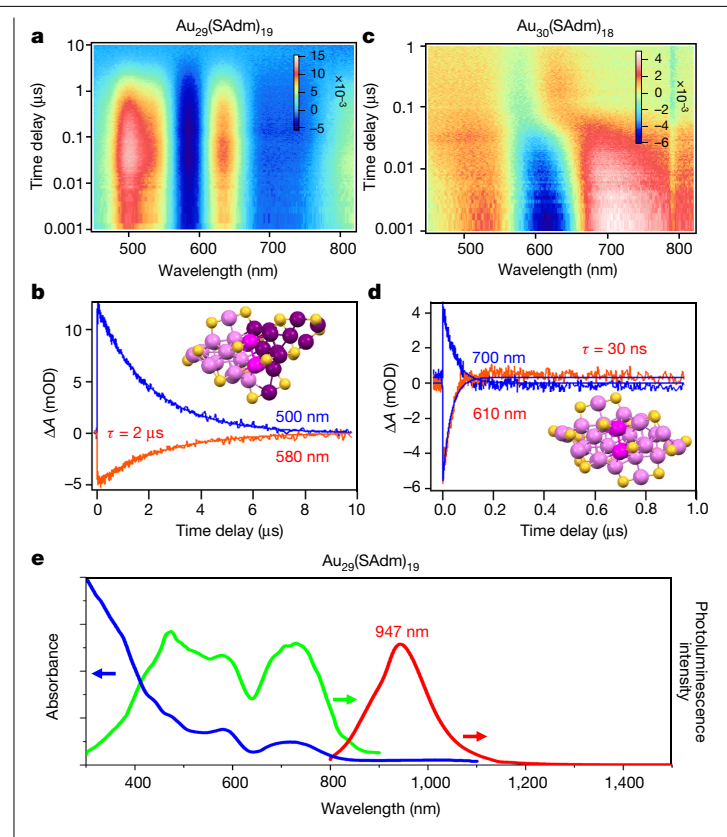


Fig. 3 | Quadruple-helical assembly of $Au_{29}(SAdm)_{19}$ nanoclusters in supercrystals. a, Self-assembly of $Au_{29}(SAdm)_{19}$ nanoclusters into a quadruple-helical structure. b, The spiral structures of two opposite strands (purple/pink) and two neighbouring strands (purple/violet and magenta/pink) in the quadruple-helical assembly. Colour codes in a, b: purple/violet/magenta/pink = Au in four strands, yellow = S, grey = C, white = H. c, Left, the central nanocluster (E2) encircled by four nanoclusters (E1) of different chirality, showing four types of interaction between two neighbouring enantiomers in the supercrystal – E2L3 – E1L1, E2L1 – E1L3, E2C3 – E1C1 and E2C1 – E1C3 (A or D layer). Right, four nanoclusters of alternative chirality, showing four types of interaction between two neighbouring enantiomers in the supercrystal – E2C3 – E1C1, E1C3 – E2C1, E2L3 – E1L1 and E1L3 – E2L1 (B or C layer). The atoms of the four different staple motifs are highlighted with larger spheres of different colours.

throughout the superlattice, forming a network in which one enantiomer coordinates with the four nearest enantiomers of opposite chirality, forming four types of interparticle interaction by matching the corresponding staple motifs, owing to the heterodimeric nature of $Au_{29}(SAdm)_{19}$.

We compared the electronic properties of the heterodimeric Au₂₉(SAdm)₁₉ and homodimeric Au₃₀(SAdm)₁₈ nanoclusters and associated structures by performing transient absorption spectroscopic analysis (pumped at 400 nm and probed between 460 nm and 820 nm) for both nanoclusters (Extended Data Fig. 9). Immediately after photoexcitation (0.6 ps), we found three ground-state bleaching (GSB) peaks at 485 nm, 580 nm and 720 nm for the heterodimeric Au₂₉(SAdm)₁₉, along with excited-state absorption (ESA) at 510 nm and 640 nm (Extended Data Fig. 9a, b). These peaks remained rather steady over the time period 10 ps to 7,000 ps (Extended Data Fig. 9c), indicating no decay of the excited state. By contrast, for the homodimeric $Au_{30}(SAdm)_{18}$, the ESA (530 nm and 720 nm) and GSB (630 nm) decayed substantially after 4 ps, and the ESA found originally at 530 nm disappeared at 7,000 ps (Extended Data Fig. 9d, e). Such a fast decay is clearly shown in the transient absorption kinetic traces (Extended Data Fig. 9f), suggesting a substantially shorter excited-state lifetime for the homodimer than for the heterodimer.

To obtain the complete excited-state lifetimes of the two nanoclusters, we carried out nanosecond transient absorption measurements (λ_{ex} = 400 nm), giving single-exponential decay lifetimes (τ) of 2 μ s for Au₂₉(SAdm)₁₉ and 30 ns for Au₃₀(SAdm)₁₈ (Fig. 4a–d). In previous



 $Fig.\,4\,|\,Comparisons\,of\,transient\,absorption\,data\,and\,carrier\,dynamics\,for$ Au₂₉(SAdm)₁₉ and Au₃₀(SAdm)₁₈ nanoclusters. a, b, Map showing nanosecond transient absorption data (a) and kinetic traces (b) for Au₂₉(SAdm)₁₉ (kinetic traces probed at 500 nm (blue) and 580 nm (red) with corresponding fits). τ, Decay lifetime. **c**, **d**, Map showing nanosecond transient absorption data (**c**) and kinetic traces (d) for Au₃₀(SAdm)₁₈ (kinetic traces probed at 690 nm (blue) and 610 nm (red) with corresponding fits). $\lambda_{\rm ex}$, 400 nm; ΔA , change in absorbance (with units of milli-optical density, mOD). e, Spectra of absorbance (blue), excitation (red, λ_{ex} = 474 nm) and emission (green, λ_{em} = 947 nm) for Au₂₉(SAdm)₁₉.

work, we reported a three-orders-of-magnitude variation in carrier lifetime between hexagonal close-packed (hcp) $Au_{30}(SAdm)_{18}(1 ns)$ and body-centred cubic (bcc) $Au_{38}S_2(SAdm)_{20}$ (4.7 µs)¹⁵. The hcp Au₃₀(SAdm)₁₈ (ref. ²⁹) and the fcc Au₃₀(SAdm)₁₈ herein are indeed a pair of isomers, indicating that the carrier lifetime is very sensitive to the structure for small-sized nanoclusters (of less than 50 Au atoms or thereabouts)30.

We further show here that fcc Au-SAdm nanoclusters with a mere difference of 'one gold in, one thiolate out' can have a remarkable 65-fold difference in carrier lifetime. The heterodimeric Au₂₉ and homodimeric Au₃₀ structures (both fcc) substantially affect the overlap of excited-state and ground-state wavefunctions: the heterodimeric structure results in much less overlap, while the homodimeric structure is symmetrical with more overlap. Owing to the long carrier lifetime of Au₂₉(SAdm)₁₉, we also tested the photoluminescence of the nanocluster solution, and observed near-infrared emission centred at 947 nm (Fig. 4e). The Au₃₀(SAdm)₁₈ solution, by contrast, does not show any near-infrared photoluminescence.

An Au₂₉(SAdm)₁₉ film made by drop casting—in which nanoclusters are randomly packed-led to moderately enhanced photoluminescence (Extended Data Fig. 9g, blue line) owing to suppression of nonradiative decays of the excited states. By contrast, the double-helical assembly of nanoclusters in supercrystals showed further enhancement of photoluminescence (Extended Data Fig. 9g, brown line), arising from the collective properties of assembly and ordered

anisotropic interactions. In DNA double helices, the π - π stacking of bases exerts electronic effects. By contrast, the adamantanthiolate ligands of Au₂₉(SAdm)₁₉ are non-aromatic and thus result in no π - π stacking, but the helical assembly still exhibits distinct effects in the photoluminescence of supercrystals owing to long-range coherence. opening new opportunities for tailoring the collective electronic properties.

Our results show that double-helical or even quadruple-helical structures can be achieved by self-assembly of heterodimeric gold nanoclusters. The intrinsically heterodimeric structure—with four surface motifs inherited from two parent nanoclusters—is responsible for the specific assembly, which results from the motif pairs formed between neighbouring nanocluster enantiomers. The precise structural matching seen in the helical assemblies stresses the advantages of using atomically precise metal nanoclusters. The asymmetric (or anisotropic) nanostructure is accompanied by different interactions in different directions on the particle surface, providing opportunities for effective tailoring of collective properties upon assembly.

Online content

Any methods, additional references, Nature Research reporting summaries, source data, extended data, supplementary information, acknowledgements, peer review information; details of author contributions and competing interests; and statements of data and code availability are available at https://doi.org/10.1038/s41586-021-03564-6.

- Srivastava, S. et al. Light-controlled self-assembly of semiconductor nanoparticles into twisted ribbons. Science 327, 1355-1359 (2010).
- Singh, G. et al. Self-assembly of magnetite nanocubes into helical superstructures. Science 345, 1149-1153 (2014).
- Shenhar, R. & Rotello, V. M. Nanoparticles: scaffolds and building blocks. Acc. Chem. Res. 36 549-561 (2003)
- Gao, Y. & Tang, Z. Design and application of inorganic nanoparticle superstructures: current status and future challenges. Small 7, 2133-2146 (2011).
- Saleh, L. M. A., Dziedzic, R. & Spokoyny, A. M. An inorganic twist in nanomaterials: making an atomically precise double helix. ACS Cent. Sci. 2, 685-686 (2016)
- Sharma, J. et al. Control of self-assembly of DNA tubules through integration of gold nanoparticles. Science 323, 112-116 (2009).
- Kuzyk, A. et al. DNA-based self-assembly of chiral plasmonic nanostructures with tailored optical response. Nature 483, 311-314 (2012).
- Chen, C.-L., Zhang, P. & Rosi, N. L. A new peptide-based method for the design and synthesis of nanoparticle superstructures: construction of highly ordered gold nanoparticle double helices. J. Am. Chem. Soc. 130, 13555-13557 (2008).
- Shen, X. et al. Rolling up gold nanoparticle-dressed DNA origami into three-dimensional plasmonic chiral nanostructures, J. Am. Chem. Soc. 134, 146-149
- Berl, V., Huc, I., Khoury, R. G., Krische, M. J. & Lehn, J.-M. Interconversion of single and double helices formed from synthetic molecular strands. Nature 407, 720-723
- Engelkamp, H. & Middelbeek, S. & Nolte, R. J. M. Self-assembly of disk-shaped molecules to coiled-coil aggregates with tunable helicity. Science 284, 785-788 (1999).
- Jin, R., Zeng, C., Zhou, M. & Chen, Y. Atomically precise colloidal metal nanoclusters and nanoparticles: fundamentals and opportunities. Chem. Rev. 116, 10346-10413 (2016).
- Li, Y., Higaki, T., Du, X, & Jin, R, Chirality and surface bonding correlation in atomically precise metal nanoclusters, Adv. Mater. 32, 1905488 (2020).
- Zeng, C., Chen, Y., Kirschbaum, K., Lambright, K. J. & Jin, R. Emergence of hierarchical structural complexities in nanoparticles and their assembly. Science 354, 1580-1584 (2016).
- 15. Zhou, M. et al. Three-orders-of-magnitude variation of carrier lifetimes with crystal phase of gold nanoclusters. Science 364, 279-282 (2019).
- Zhu, M., Aikens, C. M., Hollander, F. J., Schatz, G. C. & Jin, R. Correlating the crystal structure of a thiol-protected Au₂₅ cluster and optical properties. J. Am. Chem. Soc. 130, 5883-5885 (2008)
- Desireddy, A. et al. Ultrastable silver nanoparticles. Nature 501, 399-402 (2013)
- Macfarlane, R. J. et al. Nanoparticle superlattice engineering with DNA. Science 334.
- Li, Y. & Jin, R. Seeing ligands on nanoclusters and in their assemblies by X-ray crystallography: atomically precise nanochemistry and beyond. J. Am. Chem. Soc. 142, 13627-13644 (2020)
- Gan, Z. et al. The fourth crystallographic closest packing unveiled in the gold nanocluster crystal. Nat. Commun. 8, 14739 (2017).
- Gu, H., Zheng, R., Zhang, X. & Xu, B. Facile one-pot synthesis of bifunctional heterodimers of nanoparticles: a conjugate of quantum dot and magnetic nanoparticles. J. Am. Chem. Soc. 126, 5664-5665 (2004).

- Choi, J. et al. Biocompatible heterostructured nanoparticles for multimodal biological detection. J. Am. Chem. Soc. 128, 15982–15983 (2006).
- Brown, L. V., Sobhani, H., Lassiter, J. B., Nordlander, P. & Halas, N. J. Heterodimers: plasmonic properties of mismatched nanoparticle pairs. ACS Nano 4, 819–832 (2010).
- Buck, M. R., Bondi, J. F. & Schaak, R. E. A total-synthesis framework for the construction of high-order colloidal hybrid nanoparticles. *Nat. Chem.* 4, 37–44 (2012).
- Zhu, H. et al. Self-assembly of quantum dot-gold heterodimer nanocrystals with orientational order. Nano Lett. 18, 5049–5056 (2018).
- Xiong, L., Peng, B., Ma, Z., Wang, P. & Pei, Y. A ten-electron (10e) thiolate-protected Au₂₉(SR)₁₉ cluster: structure prediction and a 'gold-atom insertion, thiolate-group elimination' mechanism. *Nanoscale* 9, 2895–2902 (2017).
- 27. Chen, Y. et al. Isomerism in $Au_{28}(SR)_{20}$ nanocluster and stable structures. J. Am. Chem. Soc. 138, 1482–1485 (2016).
- Li, Y. et al. A correlated series of Au/Ag nanoclusters revealing the evolutionary patterns of asymmetric Ag doping. J. Am. Chem. Soc. 140, 14235–14243 (2018).
- 29. Higaki, T. et al. Controlling the atomic structure of Au_{30} nanoclusters by a ligand-based strategy. Angew. Chem. Int. Edn **55**, 6694–6697 (2016).
- Zhou, M. et al. Three-stage evolution from nonscalable to scalable optical properties of thiolate-protected gold nanoclusters. J. Am. Chem. Soc. 141, 19754–19764 (2019).

Publisher's note Springer Nature remains neutral with regard to jurisdictional claims in published maps and institutional affiliations.

© The Author(s), under exclusive licence to Springer Nature Limited 2021

Methods

Chemicals

Tetrachloroauric (III) acid (HAuCl $_4$ ·3H $_2$ O, 99.999% metal basis; Aldrich), sodium borohydride (NaBH $_4$, 99.99% metal basis; Aldrich), 1-adamantanethiol (HSAdm, HSC $_{10}$ H $_{15}$, 95%; Aldrich), tetrahydrofuran (THF, HPLC grade), ethanol (HPLC grade), methanol (HPLC grade), dichloromethane (CH $_2$ Cl $_2$, HPLC grade), acetone (HPLC grade), toluene (HPLC grade), n-hexane (HPLC grade) and thin-layer chromatography (TLC) plates (iChromatography, silica gel, 250 µm) were used as received.

Synthesis of nanoclusters

Heterodimeric Au₂₀(SAdm)₁₀ and homodimeric Au₂₀(SAdm)₁₈ as well as other adamantanethiolate-protected Au nanoclusters were prepared altogether in one batch, and then separated by TLC. We first mixed 100 mg HAuCl₄·3H₂O and 120 mg HS-Adm in methanol. After 30 min, the suspension was centrifuged and the dark orange precipitate was dissolved thoroughly in 10 ml THF for 30 min. Then, a freshly prepared aqueous solution of NaBH₄ (144 mg in 5 ml ice-cold nanopure water) was added. After 3 h, the crude product was washed thoroughly in methanol, extracted by acetone, redissolved in toluene, and stored as a solution at room temperature for incubation. A week later, the supernatant of the solution was taken by centrifugation, and the solvent was evaporated. The mixture of Au nanoclusters was extracted with CH₂Cl₂ and concentrated for TLC separation. The mixture of nanoclusters was pipetted on the TLC plate, and the separation was conducted in the developing tank (developing solvent 1:1 (v/v) CH₂Cl₂:n-hexane) for 30 min (Extended Data Fig. 1a), and the bands corresponding to different nanoclusters were cut off and dissolved in CH₂Cl₂ for characterization. Needle-shaped supercrystals of Au₂₉(SAdm)₁₉ were obtained via solvent evaporation of ethanol into a CH₂Cl₂ solution of the nanoclusters within two days; plate-shaped supercrystals of Au₃₀(SAdm)₁₈ were obtained by solvent evaporation of methanol into a CH₂Cl₂ solution of the nanoclusters within two days.

Characterization

UV-visible absorption spectra of the nanoclusters were measured on a Hewlett-Packard Agilent 8453 diode array spectrophotometer at room temperature. ESI mass spectrometry spectra were recorded using a Waters quadrupole time-of-flight (QTOF) mass spectrometer equipped with Z-Spray Source.

Femtosecond transient absorption spectroscopic measurements were carried out using a commercial Ti:sapphire laser system (Coherent, Astrella). The pump pulses in the ultraviolet and near-infrared (NIR) regions were generated by a 1.2 mJ regenerative amplifier system and optical parametric amplifier (TOPAS-Prime, Light Conversion). A small portion of the laser fundamental was focused into a sapphire plate to produce a supercontinuum in the visible range, which overlapped with the pump in time and space. Multiwavelength transient spectra were recorded at different pump–probe delay times (Helios Fire, Ultrafast Systems). Dilute solutions of metal clusters in cuvettes with a 1 mm path length were excited by the tunable output of the OPA (pump). The measurements were performed in toluene, and the optical density (OD) was adjusted to about 0.3 OD at the excitation wavelength. Nanosecond transient absorption measurements were conducted using the same ultrafast pump pulses along with an electronically delayed

supercontinuum light source with a subnanosecond pulse duration (EOS. Ultrafast Systems).

The NIR photoluminescence spectra of $Au_{29}(SAdm)_{19}$ toluene solution, film (drop casting from a concentrated solution) and supercrystals were recorded on a FS5 spectrofluorometer equipped with 500 W CW ozone-free xenon arc lamp. The spectra were measured using an excitation wavelength of 474 nm and 25 nm slits; the emission detector was an R928P photomultiplier for the UV–visible range, and an InGaSn solid-state detector for the NIR–infrared range.

X-ray crystallographic determination

A crystal of $Au_{29}(SC_{10}H_{15})_{19}$ was mounted onto a MiTeGen capillary with fluorolube, and measured using a Bruker D8 Venture with $GaK\alpha$ radiation (λ = 1.34139 Å). Data were collected under liquid nitrogen (170 K). An $Au_{30}(SC_{10}H_{15})_{18}$ crystal was measured on a Bruker APEX-II CCD diffractometer with $CuK\alpha$ radiation (λ = 1.54186 Å). The crystal was kept at 293 K during data collection. Using Olex2 (ref. 31), the structure was solved with the olex2.solve (ref. 32) structure solution program using 'charge flipping', and refined with the ShelXL 33 refinement package using least squares minimization. All Au and S atoms were found directly, and the remaining non-hydrogen atoms were generated through subsequent difference Fourier syntheses. All non-hydrogen atoms were refined anisotropically. All hydrogen atoms were set in geometrically calculated positions and refined isotropically using a riding model. The crystal information is listed in Extended Data Table 1.

Data availability

The cif files for the crystal structures of $Au_{29}(SAdm)_{19}$ and $Au_{30}(SAdm)_{18}$, and videos to show the double or quadruple helices in the $Au_{29}(SAdm)_{19}$ supercrystal, are provided as Supplementary Information with this paper. The cif files can be found at the Cambridge Crystallographic Data Centre (CCDC; https://www.ccdc.cam.ac.uk) under accession numbers 2072909 for $Au_{29}(SAdm)_{19}$ and 2072908 for $Au_{30}(SAdm)_{18}$.

- Dolomanov, O. V., Bourhis, L. J., Gildea, R. J., Howard, J. A. K. & Puschmann, H. OLEX2: a complete structure solution, refinement and analysis program. J. Appl. Cryst. 42, 339–341 (2009).
- Bourhis, L. J., Dolomanov, O. V., Gildea, R. J., Howard, J. A. K. & Puschmann, H. The anatomy of a comprehensive constrained, restrained refinement program for the modern computing environment—Olex2 dissected. Acta Crystallogr. A 71, 59–75 (2015).
- Sheldrick, G. M. SHELXT—integrated space-group and crystal-structure determination. Acta Crystallogr. A 71, 3–8 (2015).

Acknowledgements Y.L. and R.J. thank T.-Y. Luo for help in analysing crystal data. R.J. acknowledges financial support from the US National Science Foundation (NSF; grant DMR-1808675). H.W. acknowledges financial support from US Air Force Office of Scientific Research (AFOSR) award FA9550-17-1-0099. Y.S. acknowledges the startup.

Author contributions Y.L. carried out the preparation and crystallization of nanoclusters. M.Z. carried out the transient absorption measurements and analysed these data with H.W. Y.S. solved the crystal structures and measured photoluminescence. Y.L., M.Z. and R.J. wrote the manuscript, with T.H. providing suggestions.

Competing interests The authors declare no competing interests.

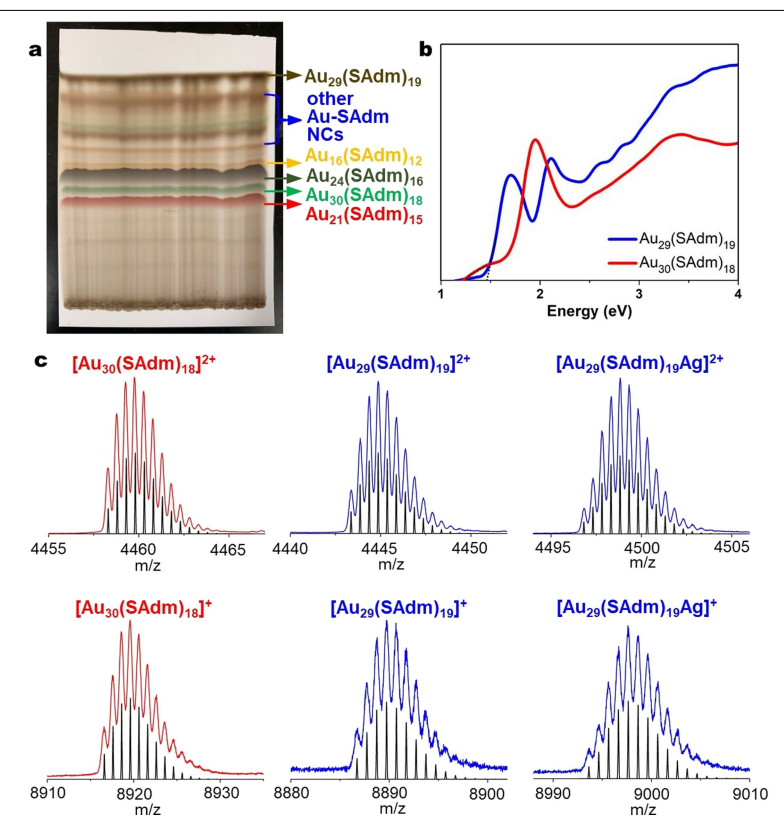
Additional information

Supplementary information The online version contains supplementary material available at https://doi.org/10.1038/s41586-021-03564-6.

Correspondence and requests for materials should be addressed to R.J.

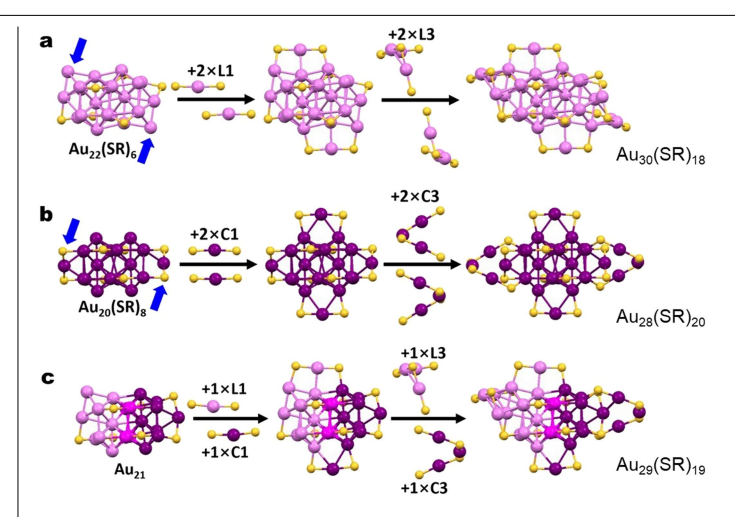
Peer review information *Nature* thanks the anonymous reviewer(s) for their contribution to the peer review of this work.

Reprints and permissions information is available at http://www.nature.com/reprints.



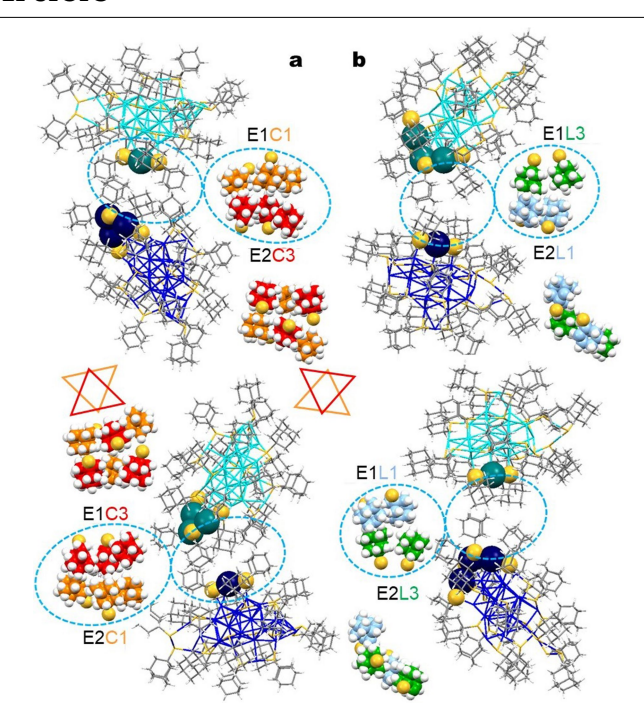
Extended Data Fig. 1| Separation by TLC and characterization of $Au_{29}(SAdm)_{19}$ and $Au_{30}(SAdm)_{18}$ nanoclusters. a, Separation of multiple Au-SAdm nanoclusters by TLC. b, Absorption spectra of heterodimeric $Au_{29}(SAdm)_{19}$ and homodimeric $Au_{30}(SAdm)_{18}$ nanoclusters on a photon energy scale. The bandgaps are determined to be 1.45 eV and 1.25 eV, respectively. c, Isotope peaks corresponding to $[Au_{30}(SAdm)_{18}]^{2+}$ and $[Au_{30}(SAdm)_{18}]^{+}$

 $(\text{red lines}), [\text{Au}_{29}(\text{SAdm})_{19}]^{2^{+}}, [\text{Au}_{29}(\text{SAdm})_{19}]^{+}, [\text{Au}_{29}(\text{SAdm})_{19}\text{Ag}]^{2^{+}} \text{ and } \\ [\text{Au}_{29}(\text{SAdm})_{19}\text{Ag}]^{+} \text{ (blue lines)}. \text{ The experimental isotopic patterns match well with the calculated ones (black lines)}. \text{ Note that the 2+ and 1+ charges are due to the ionization in ESI, and are not the native charge states of the nanoclusters}. \\ \text{In addition, an Ag cation can be picked up by Au}_{29}(\text{SAdm})_{19} \text{ during ESI-MS analysis owing to the existence of Ag}^{+} \text{ in the ion source}.$

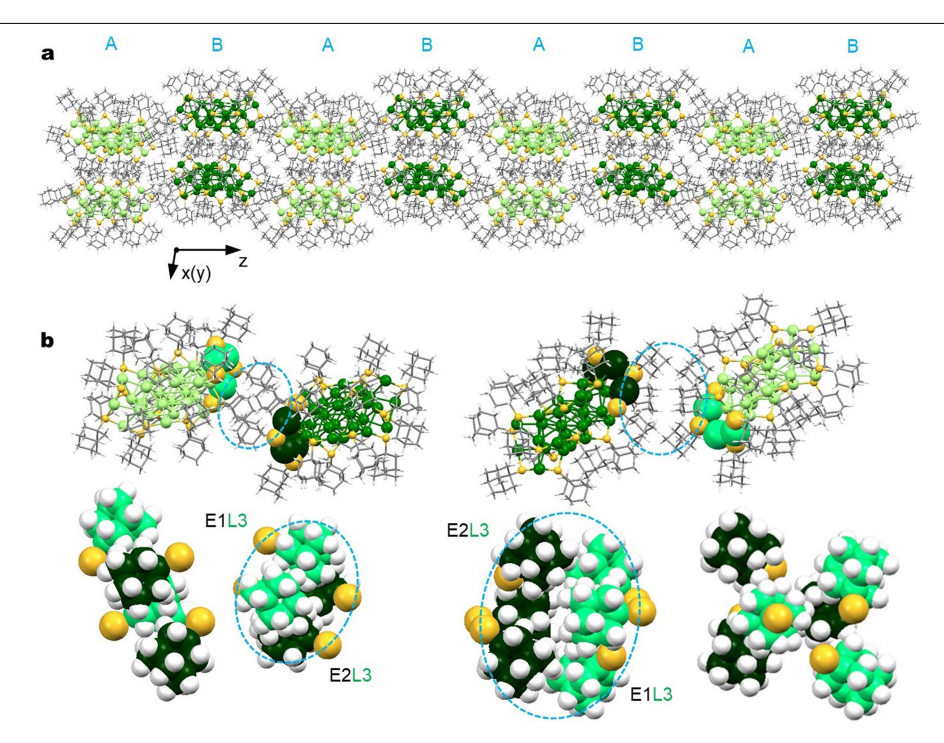


 $Extended\,Data\,Fig.\,2\,|\,An atomy\,of the\,structure\,of gold\,nan oclusters.$

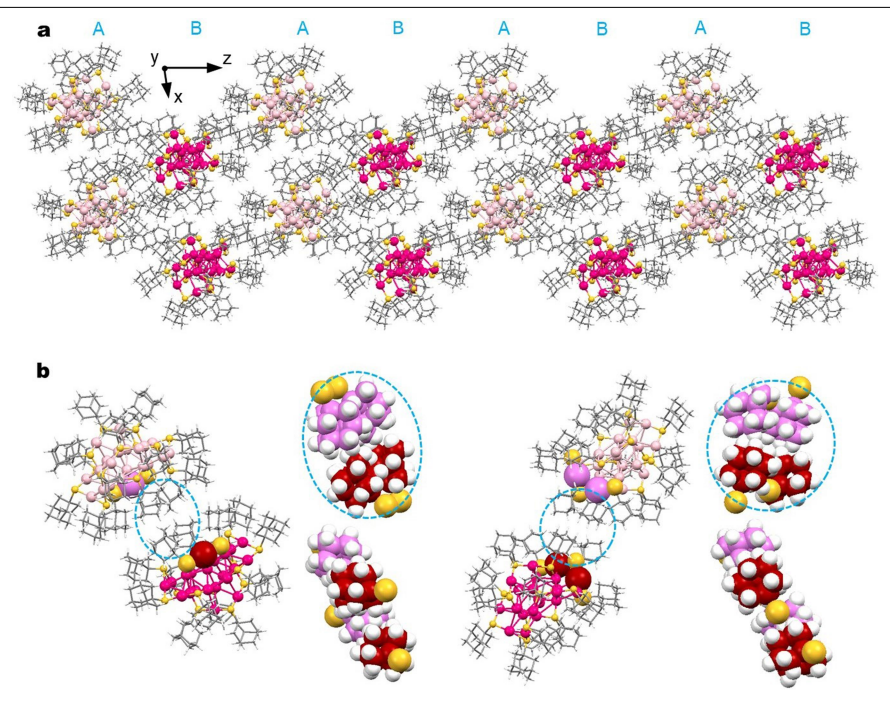
 \mathbf{a} , $\mathrm{Au_{30}(SR)_{18}}$; \mathbf{b} $\mathrm{Au_{28}(SR)_{20}}$; \mathbf{c} , $\mathrm{Au_{29}(SR)_{19}}$.



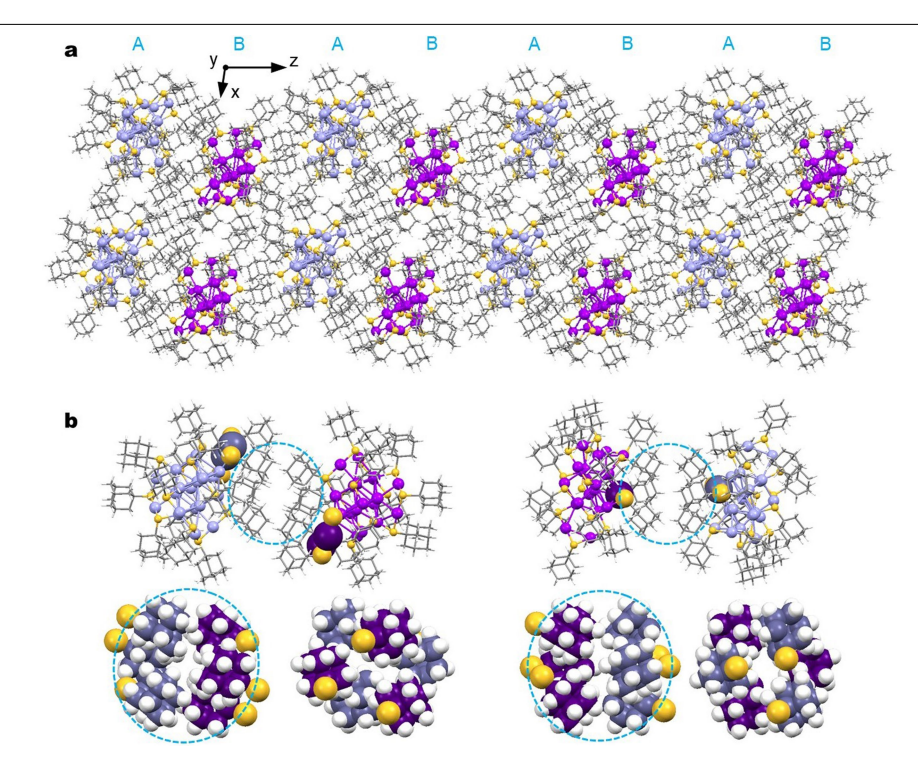
Extended Data Fig. 3 | Ligand interactions between two neighbouring $Au_{29}(SAdm)_{19}$ enantiomers. a, The triply paired ligands associated with the matching motif pairs on two neighbouring enantiomers—that is, E1C1–E2C3 and E1C3–E2C1—with interacting ligands' carbons marked in orange (for C1) and red (for C3). b, The doubly paired ligands associated with the matching motif pairs on two neighbouring enantiomers—E1L3–E2L1 and E1L1–E2L3—with interacting ligands' carbons marked in light blue (for L1) and green (for L3). In other colours: blue/cyan, Au in different enantiomers; yellow, S; grey, C; white, H.



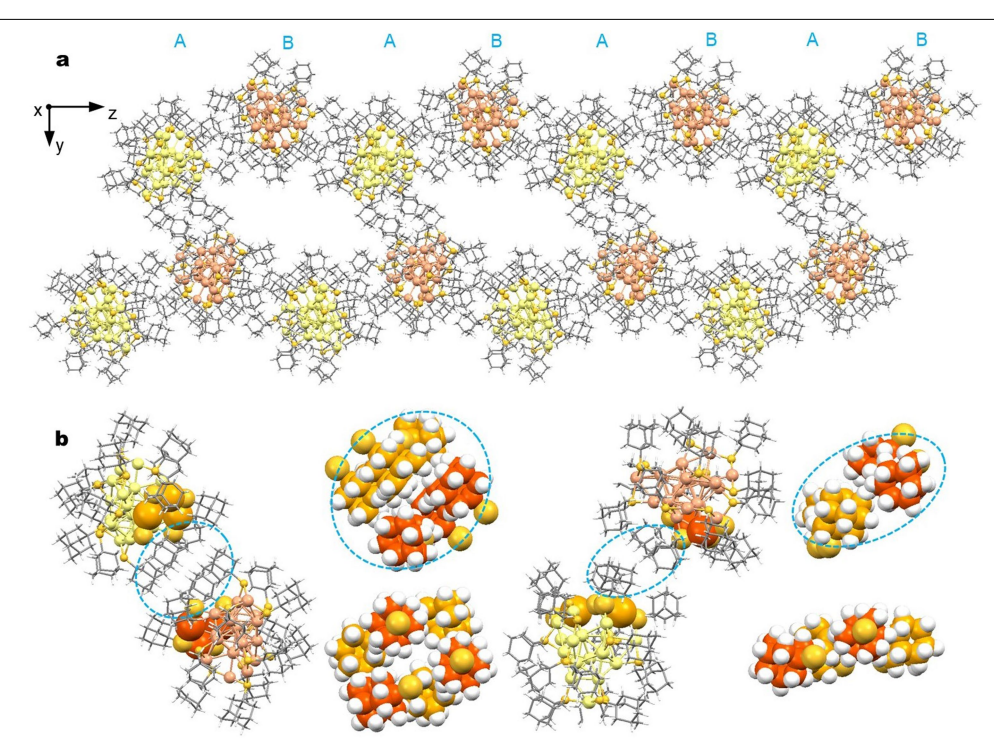
 $\textbf{Extended Data Fig. 4} | \textbf{Supercrystal of Au}_{30} \textbf{(SAdm)}_{18} \textbf{ nanoclusters. a}, \textbf{Self-assembly of Au}_{30} \textbf{(SAdm)}_{18} \textbf{ nanoclusters in the superlattice. b}, \textbf{The neighbouring enantiomers approach each other by matching their L3 staple motifs, with doubly paired and triply paired ligand interactions between the two enantiomers.}$



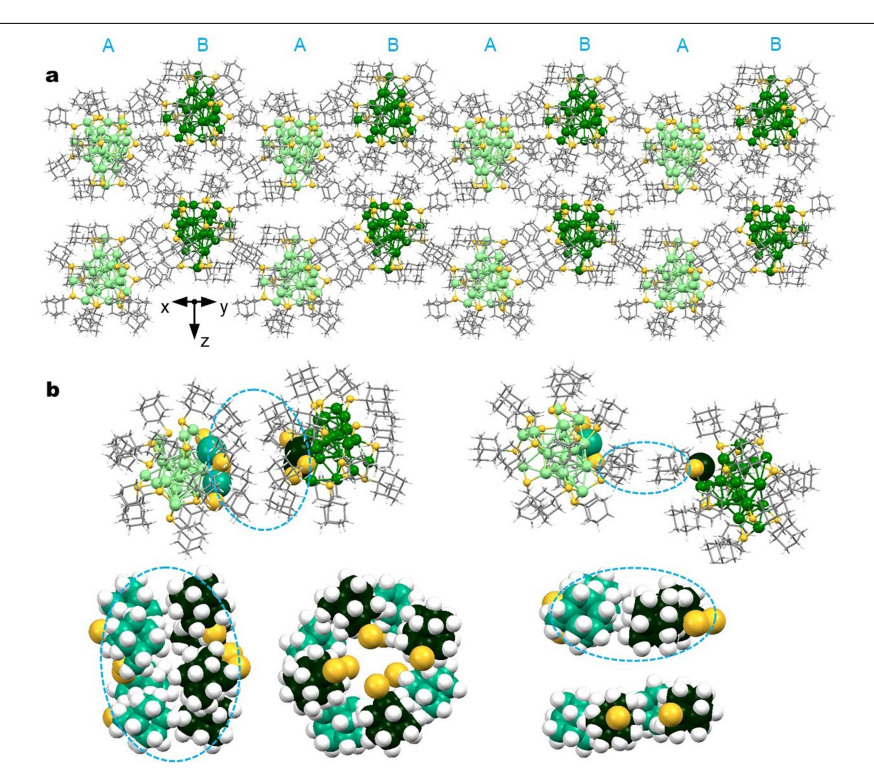
 $\textbf{Extended Data Fig. 5} | \textbf{Supercrystal of Au}_{21} (\textbf{SAdm})_{15} \textbf{nanoclusters. a}, \textbf{Self-assembly of Au}_{21} (\textbf{SAdm})_{15} \textbf{nanoclusters in the superlattice. b}, \textbf{Ligand interactions between two enantiomers. We made this figure using crystal data from ref.} \\ ^{28}.$



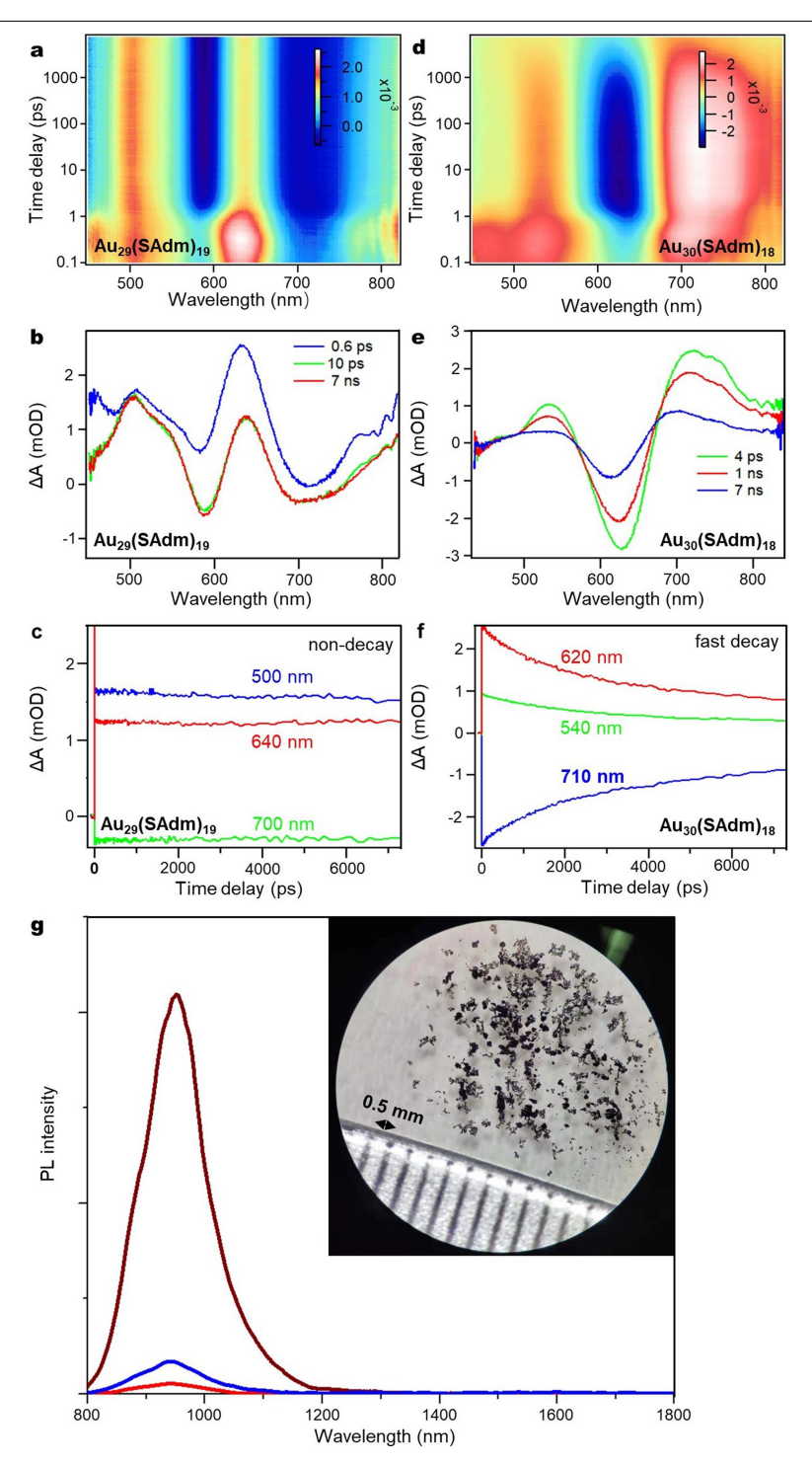
 $\textbf{Extended Data Fig. 6} | \textbf{Supercrystal of Au}_{20} \textbf{Ag}_{1} (\textbf{SAdm})_{15} \textbf{nanoclusters.a}, \textbf{Self-assembly of Au}_{20} \textbf{Ag}_{1} (\textbf{SAdm})_{15} \textbf{nanoclusters in the superlattice.b}, \textbf{Ligand interactions between two enantiomers. We made this figure using crystal data from ref.} \\ \textbf{28}.$



 $\textbf{Extended Data Fig. 7} | \textbf{Supercrystal of Au}_{19} \textbf{Ag}_{4} (\textbf{SAdm})_{15} \textbf{ nanoclusters. a}, \textbf{Self-assembly of Au}_{19} \textbf{Ag}_{4} (\textbf{SAdm})_{15} \textbf{ nanoclusters in the superlattice. b}, \textbf{Ligand interactions between two enantiomers. We made this figure using crystal data from ref.} \\ \textbf{28}.$



Extended Data Fig. 8 | **Supercrystal of Au**_{23-x}**Ag**_{<math>x}(**SAdm**)₁₅ nanoclusters (where x is approximately 7). a, Self-assembly of Au_{23-x}Ag $_x$ (SAdm)₁₅ nanoclusters (x is approximately 7) in the superlattice. b, Ligand interactions between two enantiomers. We made this figure using crystal data from ref. ²⁸.</sub>



Extended Data Fig. 9 | Maps of picosecond transient absorption data and kinetic traces of $Au_{29}(SAdm)_{19}$ and $Au_{30}(SAdm)_{18}$ nanoclusters, with NIR photoluminescence of $Au_{29}(SAdm)_{19}$, a-c, $Au_{29}(SAdm)_{19}$ (kinetic traces probed at 500 nm (blue), 630 nm (red) and 700 nm (green)). d-f, $Au_{30}(SAdm)_{18}$ (kinetic traces probed at 600 nm (blue), 700 nm (red) and 540 nm (green)).

Both nanoclusters were excited at 400 nm. ${\bf g}$, Emission spectra ($\lambda_{\rm ex}$ = 430 nm) for a solution (red; toluene solvent), film (blue; drop casting from a concentrated solution) and supercrystals (brown) of ${\bf Au}_{29}({\sf SAdm})_{19}$. Inset, photograph of ${\bf Au}_{29}({\sf SAdm})_{19}$ supercrystals under optical microscopy.

Extended Data Table 1 | Crystal data and structure refinement of $Au_{29}(SC_{10}H_{15})_{19}$ and $Au_{30}(SC_{10}H_{15})_{18}$ nanoclusters

Identification code Au₂₉(SC₁₀H₁₅)₁₉ Au₃₀(SC₁₀H₁₅)₁₈ **Empirical formula** $C_{190}H_{285}Au_{29}S_{19}$ $C_{180}H_{270}Au_{30}S_{18}$ Formula weight 8890.33 8920.02 Temperature/K 170 293(2) Crystal system orthorhombic monoclinic Space group Pbcn P2₁/n a/Å 65.1449(18) 22.0911(3) b/Å 34.1089(10) 34.5817(4) c/Å 22.6250(6) 28.8502(4) α/° 90 β/° 100.2500(10) 90 γ/° 90 90 Volume/Å³ 21688.3(5) 50273(2) 4 $\rho_{\text{calc}} g / cm^3$ 2.349 2.732 μ/mm^{-1} 23.126 38.967 F(000) 32160.0 16032.0 Crystal size/mm³ $0.1 \times 0.02 \times 0.01$ $0.05 \times 0.03 \times 0.02$ Radiation GaK α ($\lambda = 1.34139$) $CuK\alpha (\lambda = 1.54186)$ 2θ range for data collection/° 6.12 to 109.96 8.134 to 124.998 $-23 \le h \le 25, -39 \le k \le 39, -33 \le l \le 15$ $-78 \le h \le 79$, $-36 \le k \le 41$, $-17 \le l \le 27$ Index ranges Reflections collected 283043 251975 Independent reflections 47786 [$R_{int} = 0.1779$, $R_{sigma} = 0.1434$] 34324 [$R_{int} = 0.1176$, $R_{sigma} = 0.0706$] Data/restraints/parameters 47786/2541/2143 34324/2388/2053 Goodness-of-fit on F2 1.019 0.929 Final R indexes [I>=2σ (I)] $R_1 = 0.0713$, $wR_2 = 0.1479$ $R_1 = 0.0522$, $wR_2 = 0.1307$ Final R indexes [all data] $R_1 = 0.1430$, $wR_2 = 0.1734$ $R_1 = 0.0724$, $wR_2 = 0.1380$ Largest diff. peak/hole / e Å-3 4.01/-3.19 3.61/-2.23